Preprint Cambridge Centre for Computational Chemical Engineering ISSN 1473 – 4273

A new model for silicon nanoparticle synthesis

William J. Menz, Markus Kraft [1]

released: September 17, 2012

[1] Department of Chemical Engineering
and Biotechnology
University of Cambridge
New Museums Site
Pembroke Street
Cambridge, CB2 3RA
United Kingdom
E-mail: mk306@cam.ac.uk

Preprint No. 121

Keywords: silicon, parameter estimation, nanoparticles, nucleation

Edited by
Computational Modelling Group
Department of Chemical Engineering and Biotechnology
University of Cambridge
New Museums Site
Pembroke Street
Cambridge CB2 3RA
United Kingdom

Fax: + 44 (0)1223 334796
E-Mail: c4e@cam.ac.uk
World Wide Web: http://como.cheng.cam.ac.uk/

Abstract

This work presents a novel multivariate particle model to simulate the synthesis of silicon nanoparticles across a wide range of process conditions. The gas-phase mechanism of Ho et al. (1994, *J. Phys. Chem.* 98, 10138–10147) is simultaneously solved with a stochastic population balance incorporated a detailed multidimensional particle model. A systematic parameter estimation procedure is used to adjust gas-phase and heterogeneous pre-exponential factors to obtain fits with experimental results. The model is tested against a six different experimental configurations, with excellent fit observed for the majority of cases. It was found that primary particles were too large under conditions of finite-rate sintering, leading to the recommendation that the model could be made more robust by development of accurate sintering kinetics for silicon nanoparticles.

Contents

1 Introduction

Silicon nanoparticles were traditionally considered as an unwanted contaminant formed as a by-product of semiconductor manufacture [15, 47] during the thermal decomposition of silane (SiH_4). Today, they have a variety potential applications as a new material, particularly when made to a specific size and shape [2, 23, 35, 45]. As particle properties are primarily controlled by the complex decomposition mechanism of silane, it is necessary to understand the processes involved in this mechanism in order to make particles of a given diameter and morphology.

It is generally accepted that thermal decomposition of silane occurs through collision and activation of the silane molecule [25, 60, 61, 71, 74]. It then breaks-down and recombines into other silanes, silenes (doubly-bound silicon hydrides, e.g. SiH_2SiH_2, suffixed 'A') and silylenes (radical species, e.g. SiH_3SiH, suffixed 'B'), gradually increasing in size until it is treated as a particle or deposited on a surface.

This 'clustering' mechanism of gas-phase silicon hydrides has been investigated in a number of ways. For example, the decomposition of monosilane (and higher silanes) has been analysed using shock tubes [32, 74], rotating-disk reactors, [25] plasma discharge [72] and gas chromatography [3, 61]. Accompanying these studies are the numerical models of the decomposition process. Many models of varying degree of complexity have been proposed, from the 'simple' three-step reaction of Purnell and Walsh [61]; to the popular mechanism of Swihart and Girshick [71]; who proposed a mechanism containing 2615 reactions and 221 silicon hydride species, up to Si_{20}. Quantum chemical calculations and automatic mechanism generation have also been used to further develop these mechanisms [1, 75]. An excellent review of the current understanding of the silane pyrolysis mechanism and in particular, its pressure dependence, is given by Petersen and Crofton [60].

The heterogeneous reaction of silicon hydrides at silicon surfaces has also been studied in detail. Houf et al. [26] identified that silanes react with a silicon surface according to a dissociation-absorption-hydrogen mechanism, assuming that silenes and silylenes collide with surfaces with sticking coefficient of unity. Further, it was reported that the rate of evolution of hydrogen from silicon hydride surfaces is proportional to the coverage of hydrogen at the surface [26, 70]. These mechanisms were incorporated into the kinetic mechanism of Ho et al. [25] in a detailed model of the chemical vapour deposition process of silicon.

Like the gas-phase mechanism, silicon particle synthesis has been widely investigated. Early studies focused on the process conditions required to observe the onset of nucleation of particles; with a view to suppressing particle formation so as to yield higher-quality semiconductors [15, 44]. Since then, several groups have used a variety of experimental methodologies to study silicon particle synthesis.

Cannon et al. [6] used CO_2 laser heating to analyse the decomposition of silane and subsequent formation of particles in inert gases. A series of papers [7, 16, 38, 39] expanded the initial work to encompass the effect of process conditions upon particles, the properties of silicon films deposited through laser-heating of silane.

The decomposition of silane is also sensitive to specific microwave frequencies. This was

used in several studies to form photoluminescent silicon nanoparticles, or 'quantum dots' in a tubular microwave reactor [19, 23, 27]. It was reported that control of the microwave power (and therefore the temperature profile) allowed for fine adjustment of the primary particle size.

The Flagan group conducted impressively-detailed experimental studies into nucleation of silicon in single- [46, 77, 78] and multi-stage [62, 76] tubular hot-wall reactors. In all cases, different heating zones were used to tightly control the temperature profile of the reacting gas. Depending on the reactor configuration and the imposed temperature profile; particles of different size and morphology could be obtained. In typical reactor operation, it was reported that coagulation and sintering would control particle growth unless care was taken to reduce the number concentration of particles as produced by homogeneous nucleation [46].

These process conditions were recently identified by Körmer et al. [30], who produced narrowly-distributed silicon nanoparticles in a hot-wall tubular reactor with dilute silane mixtures ($\sim$ 4 %) at low pressures (2500 Pa) and high temperatures (900–1100 °C). Population balance modelling was used to confirm that heterogeneous reaction of silicon hydrides at the particle surface was predominantly responsible for particle growth [22, 31, 37].

There have been a number of other attempts to use population balance modelling to understand silicon nanoparticle formation. Nguyen and Flagan [46] used a fine-seed model to investigate the effect of pressure and temperature upon particle structure. Kruis et al. [34] employed homogeneous nucleation theory to elucidate the process conditions leading to onset of nucleation. This was expanded upon by Nijhawan et al. [47], who coupled the gas-phase mechanism of Swihart and Girshick [71] with a population balance model for a spray reactor. The kinetic mechanism of Swihart and Girshick [71] was also used in in a two-dimensional fully-coupled model incorporating the effect of fluid and particle dynamics [12, 13]; illustrating the relative importance of the various interconnected particle processes involved in synthesis.

Much work has been undertaken on the chemical and physical properties of particles obtained from silane thermal decomposition. Onischuk et al. [51] used a flow reactor to produce particles with specific hydrogen content and chemical bond structure. Subsequent works used kinetic and population balance modelling approaches to analyse kinetic pathways through which particles were formed [52, 53, 55]. Aggregate particles were studied in [54], in which particles synthesised at low temperatures under finite-rate sintering conditions. Note that the term aggregate is used here to describe chemically or sinter-bonded particles, while agglomerates refer to physically bound particles [14].

Silane decomposition at above-atmospheric pressure was addressed theoretically and experimentally by Odden et al. [48], where it was reported that particle size was independent of initial silane pressure. Additional mechanistic pathways (to the mechanism of Ho et al. [25]) were also proposed to account for the observed reaction rates at these process conditions [49, 50].

The aerosol dynamics models described previously are typically 'validated' by comparison of theoretical predictions of particle size distributions (PSDs) against those obtained experimentally. These are often obtained via direct transmission electron microscope

(TEM) imaging [30], or, in older work, though differential; mobility analysers and condensation nuclei counters [46, 77]. However, despite the wealth of information available about experimental configurations, PSDs and mechanistic pathways, no effort has been made to 'unify' the conclusions of these previous studies.

This work therefore aims to develop a new model with a detailed *type-space* to accurately predict the size and morphology of silicon nanoparticles synthesised from the thermal decomposition of silane across a range of different process conditions. A stochastic particle model coupled with a gas-phase ordinary differential equation solver is employed to achieve this. This particular modelling approach has been used for a variety of other types of nanoparticles such as soot [8, 10, 42, 56, 63, 64], silica [66–68] and titania [40, 41, 73].

The structure of this paper is as follows. The gas-phase and particle models are explained in Section 2. The parameter estimation procedure required to obtain good model fits is outlined in Section 3. The numerical results are discussed in Section 4.1, while the model predictions are compared with experimental data in Section 4.2. The paper is concluded by an evaluation of the model and discussion of further avenues for research.

2 Model development

2.1 Gas-phase kinetic model

Much study has been carried-out into the decomposition of silanes. For conditions of practical interest, the rate of decomposition of silane can be written as the bimolecular expression [60]:

$$\mathrm{SiH_4 + M \rightarrow SiH_2 + H_2 + M} \tag{1}$$

where M is a third body. It is well-understood that silane decomposition proceeds through a series of intermediate gas-phase species, such as silylene (SiH_2) and higher silenes/silanes (e.g. Si_3H_8). Thus, silicon decomposition mechanisms are often presented with many subsequent reactions after the intial decomposition step. Such examples include the work of Ho et al. [25] and Swihart and Girshick [71]. The presence of these appended 'clustering' reactions accelerates precursor decomposition [60].

This work adopts the mechanisms proposed by Ho et al. [25] to describe the chemical kinetics involved in silane decomposition and is given in full in Table 1. Note that the reactions for the species "Si" are omitted. Where appropriate, the low-pressure limit parameters (according to a Lindemann form falloff reaction) or reverse parameters are given. This mechanism was chosen in place of more recent [1, 60] or more detailed [18, 20, 71] kinetics due to sound testing at atmospheric pressure [25], relative simplicity and provision of pressure-dependent reactions.

The system of ordinary differential equations describing the reactions of Table 1 was solved using in-house developed software *Sprog* for a zero-dimensional batch reactor configuration. In order to gain better agreement with experimental data, pre-exponential factors for five reactions were adjusted. The reasons for this are discussed in Section 3.

Table 1: *Gas-phase mechanism employed. Parameters in bold have been adjusted from their original referenced values (see §3). Pre-exponentials are given with units in terms of cm, mol, s.*

no.	reaction	A	n, -	E_A, kcal/mol	ref.
1	SiH_4 (+M) $\rightleftharpoons$ SiH_2 + H_2 (+M)	3.2×10^9	1.7	54.7	[25]
	low-pressure parameters	$\mathbf{4.0 \times 10^{12}}$	0	45.1	[60]
2	Si_2H_6 (+M) $\rightleftharpoons$ SiH_4+ SiH_2 (+M)	1.8×10^{10}	1.7	50.2	[25]
	low-pressure parameters	$\mathbf{1.8 \times 10^{35}}$	-10.4	56.0	[25]
3	Si_2H_6 (+M) $\rightleftharpoons$ Si_2H_4B + H_2 (+M)	9.1×10^9	1.8	50.2	[25]
	low-pressure parameters	$\mathbf{7.8 \times 10^{40}}$	-7.8	59.0	[25]
4	Si_3H_8 (+M) $\rightleftharpoons$ SiH_2 + Si_2H_6 (+M)	7.0×10^{12}	1.0	52.7	[25]
	low-pressure parameters	8.4×10^{55}	-15.1	60.5	[25]
5	Si_3H_8 (+M) $\rightleftharpoons$ Si_2H_4B + SiH_4 (+M)	3.7×10^{12}	1.0	50.9	[25]
	low-pressure parameters	$\mathbf{4.4 \times 10^{66}}$	-17.3	59.3	[25]
6	Si_2H_4B (+M) $\rightleftharpoons$ Si_2H_4A (+M)	2.5×10^{13}	0.2	5.4	[25]
	low-pressure parameters	1.1×10^{33}	-5.8	9.2	[25]
7	Si_2H_4B + H_2 $\rightleftharpoons$ SiH_4 + SiH_2	9.4×10^{13}	0	4.1	[25]
	reverse parameters	9.4×10^{10}	1.1	5.7	[25]
8	Si_2H_4B + SiH_4 $\rightleftharpoons$ Si_2H_6 + SiH_2	1.7×10^{14}	0.4	8.9	[25]
	reverse parameters	$\mathbf{5.2 \times 10^{11}}$	0.1	8.5	[25]

2.2 Particle model

2.2.1 Type-space

Each particle P_q is represented as:

$$P_q = P_q\left(p_1, \ldots, p_{n_q}, \mathbf{C}\right) \tag{2}$$

where particle P_q contains n_q primary particles p_x. $\mathbf{C}$ is a lower-diagonal matrix representing the common surface area between two primary particles. Each primary particle is described by the number of silicon atoms η_{Si} and hydrogen atoms η_H:

$$p_x = p_x\left(\eta_{Si}, \eta_H\right) \tag{3}$$

2.2.2 Derived properties

Using the above description of particles and primaries, a number of derived properties of the silicon particles can be determined. The volume of a primary is based on the number of units η_i and bulk densities ρ_i:

$$v_x = \eta_{Si}\frac{M_{Si}}{\rho_{Si} N_A} + \eta_H \frac{M_H}{\rho_H N_A} \tag{4}$$

where M_i is the molecular weight of element i and N_A is Avogadro's number. The volume of a particle $V(P_q)$ is therefore the sum of the volume of its constituent primaries. Other derived properties are analogous to those used by Shekar et al. [67]. Of key importance is the surface area:

$$S(P_q) = \frac{S_{\text{sph}}(P_q)}{\bar{s}_q(1 - n_q^{-\frac{1}{3}}) + n_q^{-\frac{1}{3}}} \tag{5}$$

where $S_{\text{sph}}(P_q)$ is the equivalent spherical surface of a sphere with the same volume as the particle P_q, and $\bar{s}_q$ is the average sintering level between the primaries of the particle. The sintering level ($0 \leq s \leq 1$) of two primary particles p_x and p_y is given by [63]:

$$s(p_x, p_y) = \frac{\frac{S_{\text{sph}}(p_x, p_y)}{C_{xy}} - 2^{-\frac{1}{3}}}{1 - 2^{-\frac{1}{3}}}. \tag{6}$$

This definition implies that a spherical particle has a sintering level of 1, while two primaries in point contact (with no sintering) have a sintering level of 0. Mean properties of a particle are averaged over the number of primaries n_q. For example, the average primary diameter is given by:

$$\overline{d_{\text{pri}}}_q = \frac{1}{n_q} \sum_{x=1}^{n_q} d_{\text{pri}}(p_x). \tag{7}$$

The collision diameter of a particle is given by [67]:

$$d_{\text{col}}(P_q) = \overline{d_{\text{pri}}}_q \left[\frac{S(P_q)^3}{36\pi V(P_q)^2} \right]^{\frac{1}{D_f}} \tag{8}$$

where d_{pri} is the primary particle diameter and D_f is the fractal dimension. Here, D_f is assumed to have a value of 1.59; an average value from Rogak et al. [62] who studied the fractal dimension of partially sintered silicon nanoparticles. This is additionally used to estimate the mobility diameter of particles in the free-molecular regime:

$$d_{\text{mob}}^{\text{fm}} = \overline{d_{\text{pri}}}_q \sqrt{0.802(n_q - 1) + 1} \tag{9}$$

2.3 Particle processes

Particles may be created and changed according to a number of processes.

Inception: Particles are created in the population balance according to a general inception reaction, where silylene can collide with a silene or another silylene to form particles:

$$\text{Si}_i\text{H}_j\text{B} + \text{Si}_k\text{H}_l\text{X} \rightarrow P_q\,(\eta_{\text{Si}} = i + k, \eta_{\text{H}} = j + l, \mathbf{C}) \tag{10}$$

where $P_q(\eta_{\text{Si}}, \eta_{\text{H}}, \mathbf{C})$ is the $(N(t)+1)^{\text{th}}$ particle, with η_{Si} silicon atoms and η_{H} hydrogen atoms and X is A (silene) or B (silylene). This inception mechanism is

consistent with that proposed by Giunta et al. [20]. The rate of inception is given by:

$$R_{\text{incep}} = \begin{cases} \frac{1}{2} N_{\text{A}}^2 C_{\text{Si}_i\text{H}_j\text{B}} C_{\text{Si}_k\text{H}_l\text{X}} K^{\text{tr}}(\text{Si}_i\text{H}_j\text{B},\ \text{Si}_k\text{H}_l\text{X}) & d_q \geq d^* \\ 0 & d_q < d^* \end{cases} \tag{11}$$

where d_q is the incepting diameter of the particle P_q resulting from collision of species $\text{Si}_i\text{H}_j\text{B}$ and Si_kH_l, and d^* is the critical nucleus diameter, representing the theshold above which gas-phase species may convert to particles. It is calculated using the Kelvin equation [31, 34]:

$$d^* = \frac{4\gamma v_1}{k_{\text{B}} T \ln(S)}. \tag{12}$$

v_1 is the volume of silicon monomer and γ is the surface energy of silicon, given by [31]:

$$\gamma = 1.152 - 1.574 \times 10^{-4} T(\text{K}) \quad \text{N/m} \tag{13}$$

S is the supersaturation of silicon, given by the ratio of silicon partial pressure to saturation vapour pressure of silicon:

$$S = \frac{p_{\text{Si}}}{p_{\text{Si,sat}}} \tag{14}$$

In the present work, the silicon partial pressure is approximated using the sum of partial pressure of silylenes. The following correlation is used for the saturation vapour pressure [21, 31]:

$$p_{\text{Si,sat}} = 10^{7.5341 - \frac{23399}{T(\text{K})}} \quad \text{atm} \tag{15}$$

When the incepting diameter d_q exceeds the critical nucleus diameter, the rate of inception is calculated using the transition regime coagulation kernel.

Surface reaction: This work adopts a version of the 'dissociation-adsorption-hydrogen' mechanism, originally proposed by Sinniah et al. [70]. Silanes (SiH_4, Si_2H_6, Si_3H_8) react with the particle surface, releasing hydrogen. A primary p_x of particle P_q is transformed as:

$$P_q(\ldots, p_x(\eta_{\text{Si}}, \eta_{\text{H}}), \ldots, \mathbf{C}) + \text{Si}_i\text{H}_{2i+2} \rightarrow P_q(\ldots, p_x(\eta_{\text{Si}} + i, \eta_{\text{H}} + 2), \ldots, \mathbf{C}') + i\text{H}_2 \tag{16}$$

where $\mathbf{C}'$ is the new connectivity matrix resulting from the addition of surface area. The change in connectivity matrix ($\mathbf{C} \rightarrow \mathbf{C}'$) is presented by Shekar et al. [67]. The rate of surface reaction is modelled as an Arrhenius process; and is also proportional to the surface area of particle, S_q:

$$R_{\text{SR}} = A_{\text{SR,Si}_i\text{H}_{2i+2}} S_q C_{\text{Si}_i\text{H}_{2i+2}} \exp\left(-\frac{E_{\text{A,SR}}}{RT}\right) \tag{17}$$

Table 2: *Heterogeneous reaction processes included in the present work. Parameters in bold have been adjusted from their original referenced values (see §3). Surface reaction pre-exponentials have units cm/mol s, hydrogen release pre-exponentials in 1/s and condensation scaling factors are dimensionless.*

reaction	type	A	E_A, kcal/mol	ref.
$SiH_4 + p_x \rightarrow p_x(\eta_{Si}+1, \eta_H+2) + H_2$	S.R.	$\mathbf{3.0 \times 10^{33}}$	37.5	[25]
$SiH_2 + p_x \rightarrow p_x(\eta_{Si}+1, \eta_H+2)$	cond	1.0	-	[25]
$Si_2H_6 + p_x \rightarrow p_x(\eta_{Si}+2, \eta_H+2) + 2H_2$	S.R.	$\mathbf{3.0 \times 10^{34}}$	37.5	[25]
$Si_2H_4A + p_x \rightarrow p_x(\eta_{Si}+2, \eta_H+4)$	cond.	1.0	-	[25]
$Si_2H_4B + p_x \rightarrow p_x(\eta_{Si}+2, \eta_H+4)$	cond.	1.0	-	[25]
$Si_3H_8 + p_x \rightarrow p_x(\eta_{Si}+3, \eta_H+2) + 3H_2$	S.R.	$\mathbf{3.0 \times 10^{34}}$	37.5	[25]
$p_x \rightarrow p_x(\eta_{Si}, \eta_H-2) + H_2$	H_2	$\mathbf{1.2 \times 10^{19}}$	47.0	[70]

where A and E_A are the Arrhenius parameters for silane species Si_iH_{2i+2}. The Arrhenius parameters are estimated in the fitting procedure employed in the present work, explained in detail in Section 3. These reactions and parameters are given in Table 2. The Arrhenius parameters for Si_2H_6 and Si_3H_8 were set to ten times that of SiH_4, consistent with the observations of Buss et al. [5] and as done in previous models [25, 47].

Condensation: Particles can grow by the deposition of silenes and silylenes on the particle surface. The state-space of the particle is modified according to

$$P_q(\ldots, p_x(\eta_{Si}, \eta_H), \ldots, \mathbf{C}) + Si_iH_jX \rightarrow P_q(\ldots, p_x(\eta_{Si}+i, \eta_H+j), \ldots, \mathbf{C}'). \quad (18)$$

This may be modelled as a collisional process, with rate given by:

$$R_{cond} = A_{cond} C_{Si_iH_jX} \sqrt{\frac{\pi k_B T}{2 m_{Si_iH_jX}}} \left(d_{Si_iH_jX} + d_{col,q}\right)^2 \quad (19)$$

where A_{cond} is the collisional efficiency of the process (assumed 1.0, consistent with [25] for silylenes), $m_{Si_iH_jX}$ and $d_{Si_iH_jX}$ are the mass and diameter of the colliding species respectively, and $d_{col,q}$ is the collision diameter of particle q. These processes are again summarised in Table 2.

Hydrogen release: The hydrogen content of a silicon nanoparticle is a strong function of temperature and annealing time [38, 39, 70]. The present model therefore includes a stochastic jump process to account for release of hydrogen from particles:

$$P_q(\ldots, p_x(\eta_{Si}, \eta_H), \ldots, \mathbf{C}) \rightarrow P_q(\ldots, p_x(\eta_{Si}, \eta_H-2), \ldots, \mathbf{C}) + H_2 \quad (20)$$

A study of hydrogen desorption from a silicon hydride film found that the rate of desorption was first-order in coverage of hydrogen [70]. Here, the hydrogen coverage θ is estimated by the ratio of number of hydrogen atoms to silicon atoms in each particle:

$$\theta(P_q) = \frac{\sum_{x=1}^{n_q} p_x(\eta_H)}{\sum_{x=1}^{n_q} p_x(\eta_{Si})} \quad (21)$$

It is assumed that the common surface element remains unchanged due to the loss of hydrogen from the particle surface. The rate of hydrogen desorption is proportional to the coverage, given here by the ratio of number of hydrogen to number of silicon atoms:

$$R_{\mathrm{H}_2} = A_{\mathrm{H}_2}\,\theta_q \exp\left(-\frac{E_{\mathrm{A,H}_2}}{RT}\right) \tag{22}$$

The pre-exponential parameter A_{H_2} is adjusted according to the methodology in Section 3, and $E_{\mathrm{A,H}_2}$ is given in Table 2

Coagulation: Coagulation of particles results in the following change to the state space:

$$P_q\left(p_1,\ldots,p_{n_q},\mathbf{C}_q\right) + P_r\left(p_1,\ldots,p_{n_r},\mathbf{C}_r\right) \rightarrow P_s\left(p_1,\ldots,p_{n_q},p_{n_q+1},\ldots,p_{n_q+n_s},\mathbf{C}_s\right) \tag{23}$$

The rate of coagulation is calculated using the 'transition regime coagulation kernel', which is a computationally efficient approximation to true Brownian coagulation [36]. The transition regime coagulation kernel $K^{\mathrm{tr}}(P_q,P_r)$ is the harmonic average of the slip-flow kernel and free-molecular kernel:

$$K^{\mathrm{tr}}(P_q,P_r) = \left(\frac{1}{K^{\mathrm{fm}}(P_q,P_r)} + \frac{1}{K^{\mathrm{sf}}(P_q,P_r)}\right)^{-1}. \tag{24}$$

The free-molecular kernel $K^{\mathrm{fm}}(P_q,P_r)$ is dominant for $\mathrm{Kn} \gg 1$:

$$K^{\mathrm{fm}}(P_q,P_r) = 2.2\sqrt{\frac{\pi k_{\mathrm{B}} T}{2}}\left(\frac{1}{m_q}+\frac{1}{m_r}\right)^{\frac{1}{2}}\left(d_{\mathrm{col},q}+d_{\mathrm{col},r}\right)^2 \tag{25}$$

where m_q is the mass of particle P_q. After substitution of the Cunningham slip correction factor and the Knudsen number, the slip flow kernel is given by

$$K^{\mathrm{sf}}(P_q,P_r) = \frac{2\,k_{\mathrm{B}}\,T\left(d_{\mathrm{col},q}+d_{\mathrm{col},r}\right)}{3\,\mu}\left(\frac{1}{d_{\mathrm{col},q}}+\frac{1}{d_{\mathrm{col},r}}+1.257(2\sigma)\left[\frac{1}{d_{\mathrm{col},q}^2}+\frac{1}{d_{\mathrm{col},r}^2}\right]\right) \tag{26}$$

where μ is the gas viscosity and σ is the mean-free path of gas molecules.

The common-surface matrix $\mathbf{C}$ is changed to reflect the structure of old particles P_q and P_s, and their new connection. The process through which this is done is described in detail by Shekar et al. [67].

Sintering: Sintering is implemented using the exponential excess surface area decay formula, as popularised by Koch & Friedlander [29]:

$$\frac{\Delta C_{xy}}{\Delta t} = -\frac{1}{\tau_{\mathrm{S}}(p_x,p_y)}\left(C_{xy} - S_{\mathrm{sph}}(p_x,p_y)\right) \tag{27}$$

where C_{xy} represents the element of the common-surface matrix $\mathbf{C}$ describing the common surface area of the two primaries p_x and p_y, and $S_{\mathrm{sph}}(p_x,p_y)$ is their equivalent surface area. The characteristic sintering time is an empirical function of T and

Table 3: *Numerical and model parameters used in the present work.*

description	symbol	value	ref.
Numerical parameters			
Maximum splitting timestep	Δt_s	2.5×10^{-4} s	[67]
Maximum number of stochastic particles	$N_{\max}$	16,384	[36]
Number of runs	L	8	[36]
Model parameters			
Maximum zeroth moment	$M_{0,\max}$	1.0×10^{14} #/m^3	-
Sintering pre-exponential	A_S	1.15×10^{13} s/m^4	[33]
Sintering temperature power	n_S	4	[33]
Sintering characteristic energy	E_S	55.0 kcal/mol	[33]
Density of silicon	ρ_{Si}	2329 kg/m^3	-
Density of hydrogen	ρ_H	101 kg/m^3	-
Process settings			
Temperature range	T	800–1400 °C	-
Residence time range	τ	0.001–1.0 s	-
Initial fraction of SiH_4 range	y_{SiH_4}	0.0004–1.0	-
Total pressure range	P	2500–101,325 Pa	-

d which is related to the time required for a two neighbouring primaries to coalesce. It is typically expressed in the form:

$$\tau_S = A_S \, d^{n_S} \, T \exp\left(\frac{E_S}{RT}\right) \tag{28}$$

where A_S, n_S and E_S are empirical parameters. Here, the sintering parameters quoted by Kruis et al. [33] adapted from the titania grain-boundary diffusion [28] model are used. These are preferred over those of [79] as the latter set of kinetics predict coalescence of particles for conditions of practical interest [37].

2.4 Coupling algorithm

The gas-phase kinetic model and the stochastic particle population balance are coupled using an operator-splitting algorithm with Strang splitting [8, 9]. The Linear Process Deferment Algorithm is used to accelerate linear processes such as surface reaction and condensation [57]. The full algorithm though which this occurs for an analogous particle model is described by Shekar et al. [67]. The numerical and model parameters used for the fully-coupled model are summarised in Table 3.

3 Parameter estimation

Previous studies have identified that, at low pressure, use of literature gas-phase mechanisms (e.g. that of Swihart and Girshick [71]) requires scaling of either the gas-phase pre-exponentials [22, 31, 37] or scaling of the nucleation rate [47]. In some cases, both the kinetic parameters and nucleation rates (via usage of collision efficiencies) were empirically adjusted to obtain model fits [54, 55]. Thus, it is necessary to chose appropriate model parameters to ensure theoretical results are comparable with experimental results.

Of the reactions included in the gas-phase mechanisms, Petersen and Crofton [60] noted that the silane and silylene concentration was most sensitive to reactions 1 and 7. Onischuk et al. [55] additionally reported that fitting of reactions 1 and 3 was required for their population balance model. Preliminary calculations for this work indicated that adjustment of the pre-exponentials of reaction 5 and reaction 8 (reverse) was necessary to achieve agreement with experimental work. As silane decomposition occurs at the low-pressure limit [60] up to 5 atm the low-pressure pre-exponentials were adjusted, where available.

As in previous studies, the surface reaction [22, 31, 37] and hydrogen release [55] rates were adjusted via the pre-exponential factors. In total, there are seven parameters which require estimation. This system's parameter vector is therefore given by

$$\mathbf{x} = \left(A_{1,\mathrm{LP}},\, A_{2,\mathrm{LP}},\, A_{3,\mathrm{LP}},\, A_{5,\mathrm{LP}},\, A_{8,\mathrm{rev}},\, A_{\mathrm{SR,SiH_4}},\, A_{\mathrm{H_2}}\right)\,. \tag{29}$$

To choose an appropriate set of parameters $\mathbf{x}$, a staged optimisation methodology analogous to those given in [37] was employed. Firstly, low-discrepancy (Sobol) sequences were used to located four parameter sets close to minima, as defined by objective function $\Phi(\mathbf{x})$:

$$\Phi(\mathbf{x}) = \sum_{i=1}^{N_{\mathrm{exp}}} \left(\phi_i^{\mathrm{exp}} - \phi_i^{\mathrm{sim}}(\mathbf{x})\right)^2. \tag{30}$$

where ϕ_i represents one of the datasets used in fitting, listed in Table 4. A selection of studies using a range of process conditions were used, and equal weighting was applied to each of the datasets used in the objective function. The bounds for the Sobol scans were found empirically. The four best parameter sets from the initial parameter space scan are further refined by applying the simultaneous stochastic approximation algorithm (SPSA) [24]; the best of which $\mathbf{x}^*$ is chosen according to

$$\mathbf{x}^* = \arg\min_x \left\{\Phi(\mathbf{x})\right\}. \tag{31}$$

The optimal set of parameters is obtained via use of the Bayesian approach of Mosbach et al. [43] and Braumann et al. [4]. Using an Inverse-Wishart prior (as the error in the experimental values is unknown), a Metropolis-Hastings algorithm is employed to estimate the posterior distribution of the parameters. A fourth-order response surface was constructed locally around the point $\mathbf{x}^*$ in order to reduce the time needed for the many model evaluations in the sampling algorithm. This methodology provides an estimate of the modal value of each parameter in $\mathbf{x}$ and its corresponding uncertainty.

Table 4: *Experimental data used in fitting the model. $\sigma_a(d_{pri})$ refers to the arithmetic standard deviation of the primary diameter.*

i	T, °C	y_{SiH_4}, %	P, kPa	τ, s	ϕ_i	ϕ_i^{exp}, nm	ref.
1	1100	4.0	2.5	0.08	$d_{pri,mode}$	26.7	[30]
2	1100	4.0	2.5	0.08	$\sigma_a(d_{pri})$	1.7	[30]
3	1100	4.0	2.5	0.08	$d_{pri,10}$	24.1	[30]
4	1100	4.0	2.5	0.08	$d_{pri,90}$	28.8	[30]
5	900	4.0	2.5	0.42	$d_{pri,mode}$	21.2	[30]
6	580	5.0	39.0	0.53	$d_{pri,mode}$	41.0	[54]
7	816	3.3	51.0	0.0026	$d_{pri,mode}$	11.0	[18]
8	1047	3.3	51.0	0.0021	$d_{pri,mode}$	11.0	[18]

Table 5: *Optimal parameters obtained from the parameter estimation procedure. The mode, upper and lower bounds are those of the high probability density region for a 99.99% credible interval.*

parameter	units	lower bound	mode	upper bound
$A_{1,LP}$	cm^3/mol.s	3.2×10^{12}	4.0×10^{12}	5.8×10^{12}
$A_{2,LP}$	cm^3/mol.s	3.8×10^{33}	1.8×10^{35}	2.8×10^{37}
$A_{3,LP}$	cm^3/mol.s	2.1×10^{39}	7.8×10^{40}	1.8×10^{43}
$A_{5,LP}$	cm^3/mol.s	1.7×10^{54}	8.4×10^{55}	1.4×10^{58}
$A_{8,rev}$	cm^3/mol.s	8.1×10^{10}	5.2×10^{11}	7.0×10^{13}
A_{SR,SiH_4}	cm/mol.s	1.1×10^{33}	3.0×10^{33}	1.3×10^{34}
A_{H_2}	1/s	1.2×10^{19}	3.08×10^{20}	6.3×10^{20}

4 Results and discussion

4.1 Numerical results

The model parameters and their credible intervals as obtained from the parameter estimation procedure are given in Table 5. A qualitative understanding of sensitivity of the objective function $\Phi(\mathbf{x})$ to each parameter can be gained from this information. For example, the credible intervals of $A_{1,LP}$ and A_{SR,SiH_4} are within an order of magnitude of the modal value, indicating that the accuracy of the model is strongly dependent on correct estimation of these values. In comparison, the bounds for $A_{3,LP}$ span four orders of magnitude, suggesting that $\Phi(\mathbf{x})$ is less sensitive to this value.

As the objective function is very sensitive to reaction 1 and previous studies [60] have identified it as the most important step in governing the decomposition rate, it is worthwhile discussing the value of $A_{1,LP}$ obtained here through model-fitting. Table 6 lists the low-pressure parameters for reaction 1 for several other studies: one used in a mechanism to describe chemical vapour deposition (CVD) of silane [25], another obtained through detailed experimental studies [60], and the others used for coupling with particle models [18, 31, 37, 58].

Table 6: *Comparison of other kinetic expressions for the low-pressure limit of reaction 1.*

study	A, cm^3/mol.s	n, -	E_A, kcal/mol
Ho et al. [25]	5.2×10^{29}	-3.5	57.6
Frenklach et al. [18]	5.9×10^{41}	-8.8	67.2
Petersen and Crofton [60]	7.2×10^{15}	0	45.1
Paur et al. [58]	1.3×10^{12}	0.68	58.0
Körmer et al. [31]	9.0×10^{12}	0	45.1
Menz et al. [37]	5.1×10^{10}	0	45.1
this work	4.0×10^{12}	0	45.1

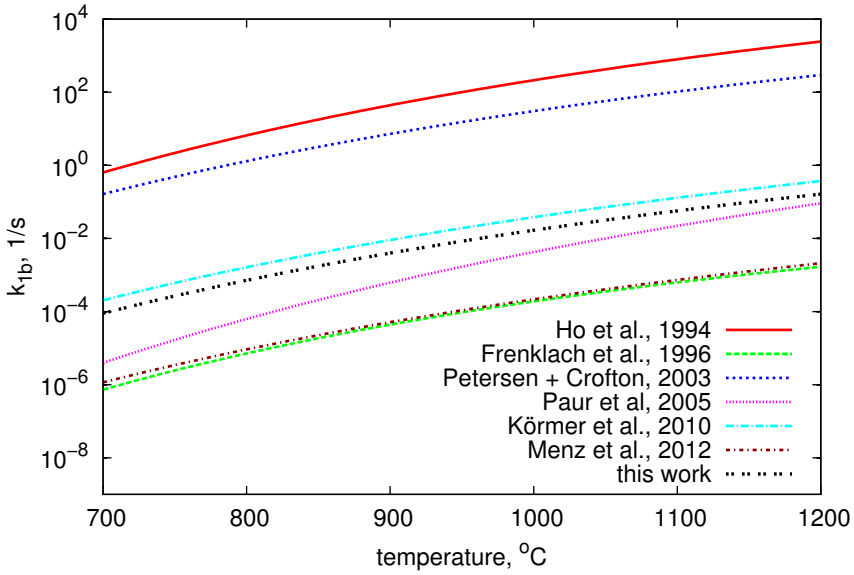

Figure 1: *Dependence of the unimolecular rate constant (k_{1b}) upon temperature at 2.5 kPa (conditions of Körmer et al. [30]) for a variety of literature kinetic models.*

There is clearly a large variation in values of the pre-exponential, especially when the additional temperature fitting power n is used. It is useful to use unimolecular rate constant (k_{1b}) when comparing the reaction rates predicted by each set of parameters [60]. Here, it is given by:

$$\frac{\mathrm{d}C_{\mathrm{SiH_4}}}{\mathrm{d}t} = -k_1 C_{\mathrm{SiH_4}} C_M = -k_{1b} C_{\mathrm{SiH_4}} \tag{32}$$

This rate constant is compared across the kinetic models of Table 6 in Figure 1. It is evident that the rate constants in pure gas-phase models (e.g. [25, 60]) are three to four orders of magnitude greater than those coupled to particle models [18, 31, 37, 58]. Even within the set of those coupled to particle models, the unimolecular rate constant spans three orders of magnitude. The rate expression found in the present work from parameter estimation appears to correspond well with that of Körmer et al. [31].

It is hypothesised that k_{1b} reported here is approximately two orders of magnitude greater than the 'slowest' depicted [18, 37] due to the inclusion of the homogeneous nucleation

Table 7: *Experimental data and corresponding process conditions used in the present work.*

study	reactor	T, °C	y_{SiH_4}, %	P, kPa (bath)	τ, s
Flint et al. [17]	Laser	700–1000	0.21	20 (Ar)	0.005
Wu et al. [78]	PFR	450–1200	1.0	101 (N_2)	1.0
Nguyen and Flagan [46]	PFR	500–1200	0.04–1.0	101 (N_2)	0.9
Frenklach et al. [18]	Shock tube	816–1307	3.3	51 (Ar)	0.001–0.0026
Onischuk et al. [54]	PFR	580	5.0	39 (Ar)	0.2–0.8
Körmer et al. [30]	PFR	500–1100	2.0–13.0	2.5 (Ar)	0.08–0.42

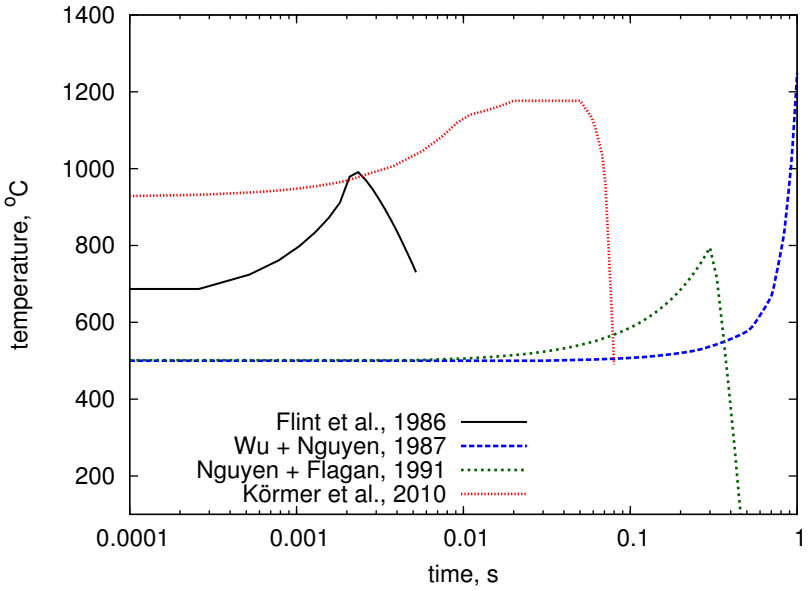

Figure 2: *Experimental temperature profiles used in the model calculations for the case studies of Table 7.*

criterion in the rate equation for inception (Equation (11)).

The authors also note the good agreement of A_{SR,SiH_4} with the value proposed by Houf et al. [26] and used in the gas-surface mechanism Ho et al. [25] after conversion from *SURFACE CHEMKIN* [11] to the type-space of the present work. This is discussed in Appendix A.

4.2 Case studies

There is an overwhelming amount of literature which describes the production of silicon nanoparticles under a variety of process conditions. Several of these cases representing different types of particles or reactor configurations were selected, and those studied in the present work are displayed in Table 7. Where available, published temperature profiles were used (e.g. [78]), given in Figure 2.

All profiles (e.g. temperature versus length in [17]) were converted from length coordinates to time coordinates assuming plug flow and volumetric flowrates, unless a residence time was supplied. In the cases with no temperature profile (e.g. [54]), the time corresponds to a 'hot-zone' residence time; and a constant temperature was used. Particle size distributions (PSDs) are the number-density distributions and were generated using kernel density estimation and the normal distribution approximation to estimate the bandwidth [69].

4.2.1 Narrow PSDs

Narrowly-distributed particles are obtained when inception occurs for a very short period of time, coagulation is negligible, and particles are grown by heterogeneous deposition [31, 37]. A detailed study of the production of uniform silicon nanoparticles was conducted by Körmer et al. [30], where particle size could be controlled between 20 and 40 nm through choice of process conditions.

Under these conditions, much of the precursor is lost to the wall due to vapour deposition on the reactor surface. In a similar vein to [22], this work assumes that only 16% of the initial precursor reacts to form particles. A temperature profile similar to the optimsed profile of Gröschel et al. [22] is used for the 84 ms, 1100 °C cases, given in Figure 2. The model predictions and experimental results for this system are compared in Figure 3.

As previously identified [22, 31, 37], negligible coagulation should occur in order to obtain a narrow size distribution. There is reasonable agreement between the model and literature results, especially for greater silane fractions. The secondary and very small tertiary peaks for the 'base case' is a result of particles coagulating once or twice. For the higher silane fraction cases, much more silicon in the particle phase yields many more coagulation events, broadening the distribution and 'smoothing-out' the additional modal peaks.

At long residence times ($\tau \sim 420$ ms) the PSDs predicted by the model are far too broad as compared to those observed experimentally [30]. It is evident that in these cases, the model either over-predicts the rate of coagulation or is not capturing some aspect of detail of the real process. As this system is particularly sensitive to the temperature profile imposed [22], it is possible that the longer residence time cases require further experimental characterisation.

Nucleation of silicon particles in a shock tube was studied by Frenklach et al. [18]. Spherical particles with sizes between 10 and 40 nm and narrow size distributions were produced in the shock tube at a range of process conditions. Experimental PSDs were reported for a 3.3% SiH_4-Ar mixture with a total pressure of 0.5 atm, and are compared to the theoretical predictions in Figure 4.

Very good agreement of theoretical and experimental PSDs is observed for the 816 °C and 1307 °C cases. However, the modal diameter for the 1047 °C case is approximately double that reported in [18]. In a similar vein to the 420 ms cases of Körmer et al. [30] described previously, the broadening observed in this case is associated with too much coagulation.

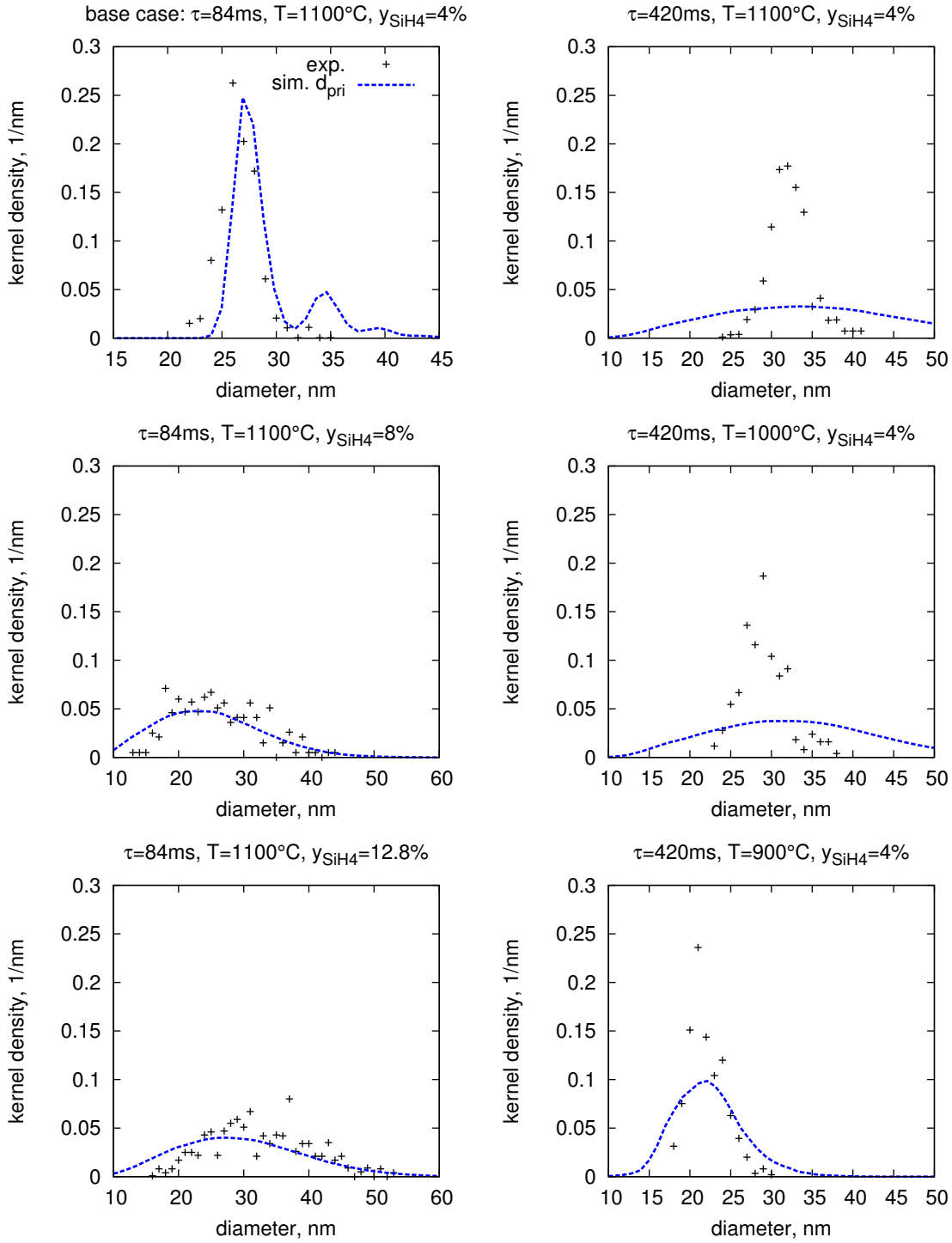

Figure 3: *Comparison of the experimental PSDs of Körmer et al. [30] at 25 kPa total pressure (in Ar) and those predicted by the present model.*

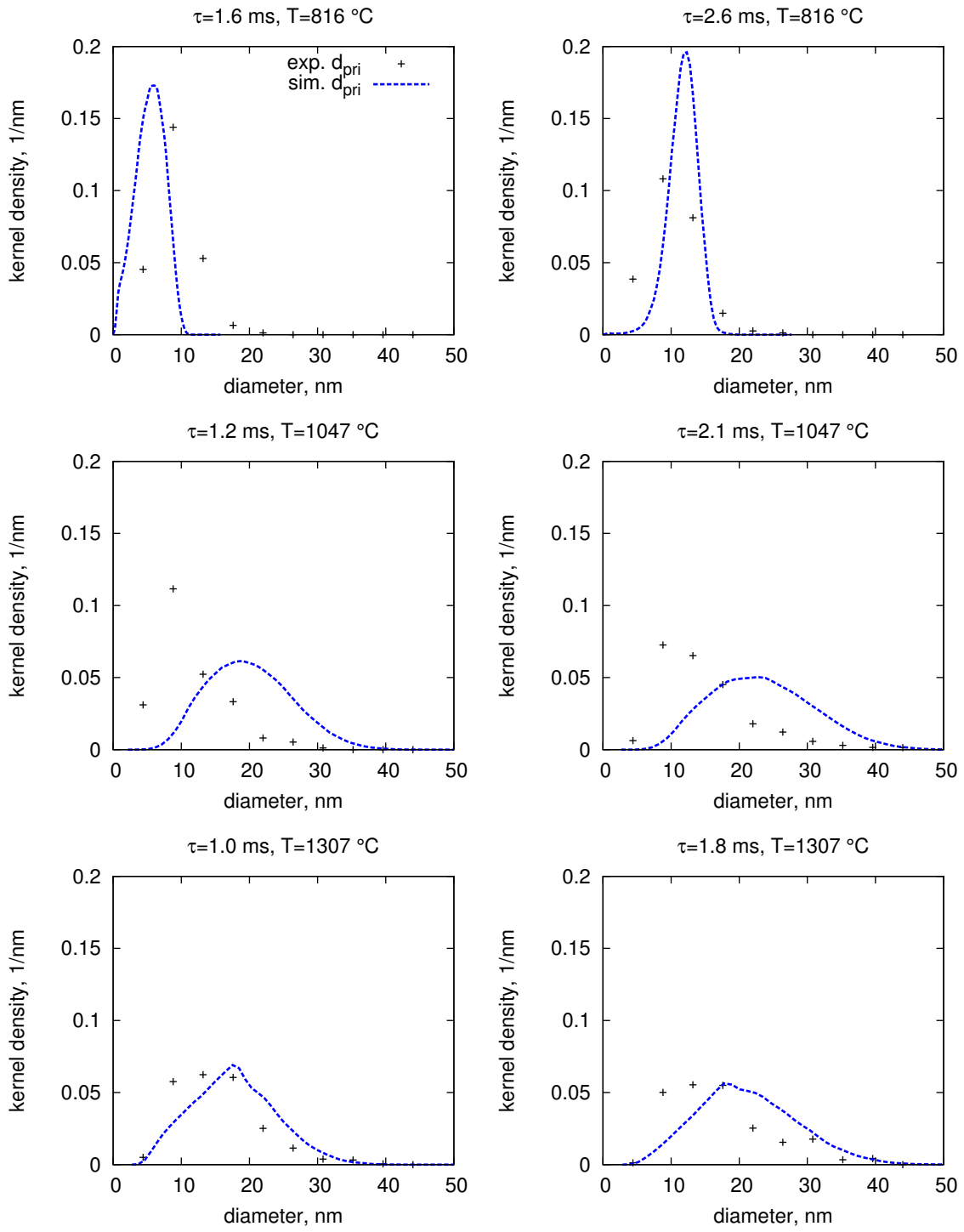

Figure 4: *Comparison of theoretical and experimental PSDs for the shock tube reactor of Frenklach et al. [18] with initial conditions y_{SiH_4}=3.3% (in Ar) and P=51 kPa.*

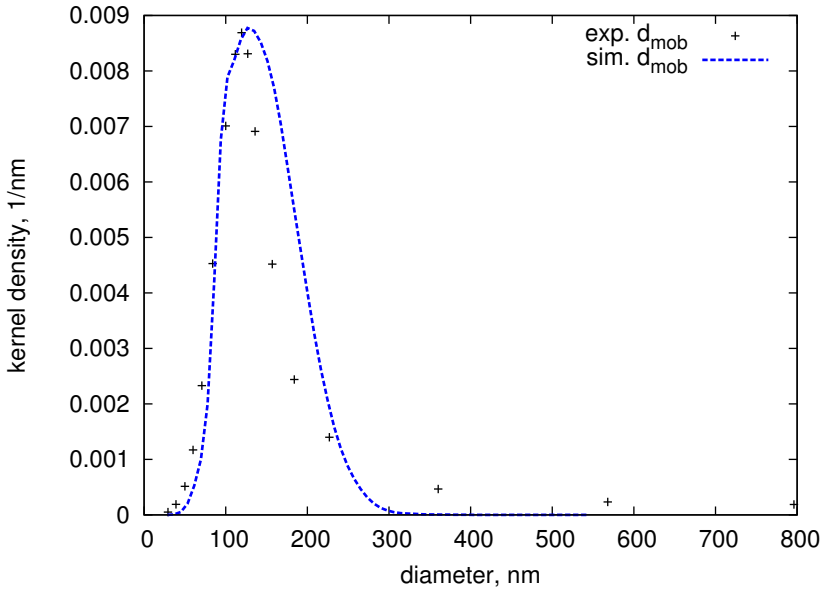

Figure 5: *Comparison of theoretical and experimental PSDs for the system of Wu et al. [78] with initial conditions $y_{SiH_4} = 1.0\%$ (in N_2) at atmospheric pressure.*

4.2.2 Sintered particles

Wu et al. [78] used a tubular reactor to generate highly-spherical crystalline silicon particles through coagulation and sintering of smaller particles at a high temperature. A peak temperature of 1200 °C (temperature profile given in Figure 2) and initial silane fraction of 1 % at atmospheric pressure (in nitrogen) was required to achieve these particles. The resulting particle size distribution is given in Figure 5.

The model predictions show excellent agreement with the experimental PSD. The particles predicted by the model are completely spherical, with a geometric standard deviation of 1.50, indicating that the particle size distribution is at the self-preserving limit. The model is also able to provide additional physical insight into this particular case: Figure 6 shows the temporal evolution of the primary and collision diameter for this system.

It is evident that while particles are initially spherical ($d_{\text{col}} = d_{\text{pri}}$), these measurements begin to diverge after 0.4 s. This phenomenon is a result of much coagulation of particles, as illustrated by renderings of the particles at the specified times. By the end of the residence time, the high temperature has caused coalescence, yielding spherical particles. This is in agreement with the hypothesis of Nguyen and Flagan [46] that particle growth occurred by vapour deposition (surface reaction), cluster deposition (condensation) and coagulation, rather than the pure condensation process proposed in [78].

4.2.3 Particle aggregates

Particle synthesis under conditions of finite-rate sintering was experimentally and theoretically investigated by Nguyen and Flagan [46]. Using a single-stage tubular reactor, they investigated formation of aggregates at different silane concentrations (0.01–1.0%) with a

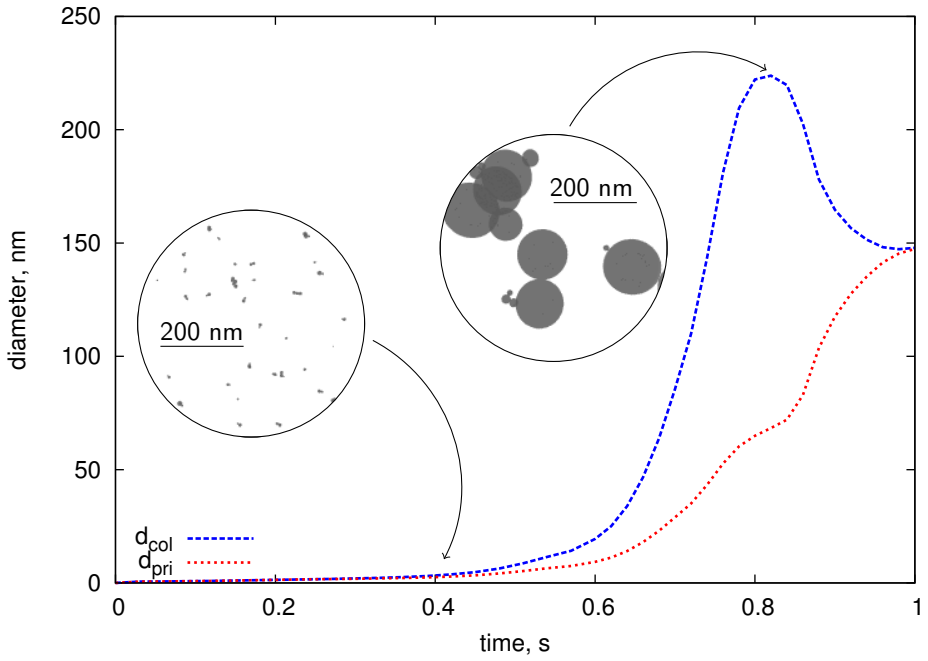

Figure 6: *Evolution of the mean primary and collision diameters for the case of Wu et al. [78]. Insets depict snapshots of the particle ensembles at 0.4 s and 0.8 s. Particle images were rendered using POV-Ray [59].*

lower peak reactor temperature as compared to Wu et al. [78]. This reactor was operated at atmospheric pressure with nitrogen as the bath gas. Their results are compared to those predicted by the present model in Figures 7 and 8.

It is evident that the theoretically-predicted average mobility diameter and the mobility diameter particle size distributions (Figure 8) are in good agreement with the experimental data. However the primary diameter is too large for silane concentrations above 0.07% (Figure 7. This is attributed to the sintering kinetics used; which remain untested in population balances [37].

The formation of particle aggregates was also identified by Onischuk et al. [54] in a detailed examination of the nature of particle structures obtained when sampling from the 'hot-' and 'cold-zones' of the reactor. Aggregates were sampled from inside the reactor corresponding to various hot-zone residence times and their primary particle structure analysed. The model and experimental results are compared in Figure 9 for a constant temperature of 580 °C and initial conditions of 5 % silane in argon at 39 kPa.

Excellent agreement is observed between the model predictions of the temporal evolution of the average primary diameter and the experimental results. In order to compare particle aggregates, a TEM-style image was generated by assuming that primary particles randomly adhere to each other (Figure 10). Here, it is clear that there is at least qualitative agreement with aggregate size and structure.

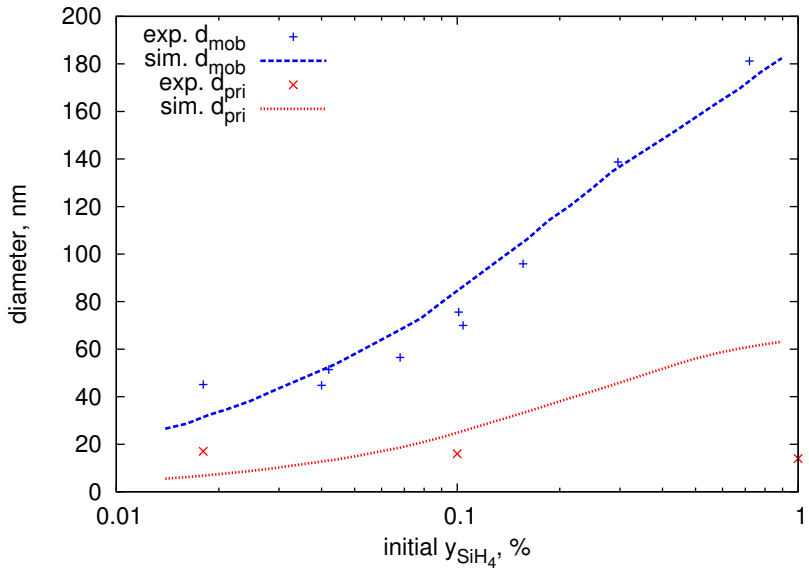

Figure 7: *Dependence of particle size on intial precursor concentration for the system of Nguyen and Flagan [46] with a peak reactor temperature of 800 °C.*

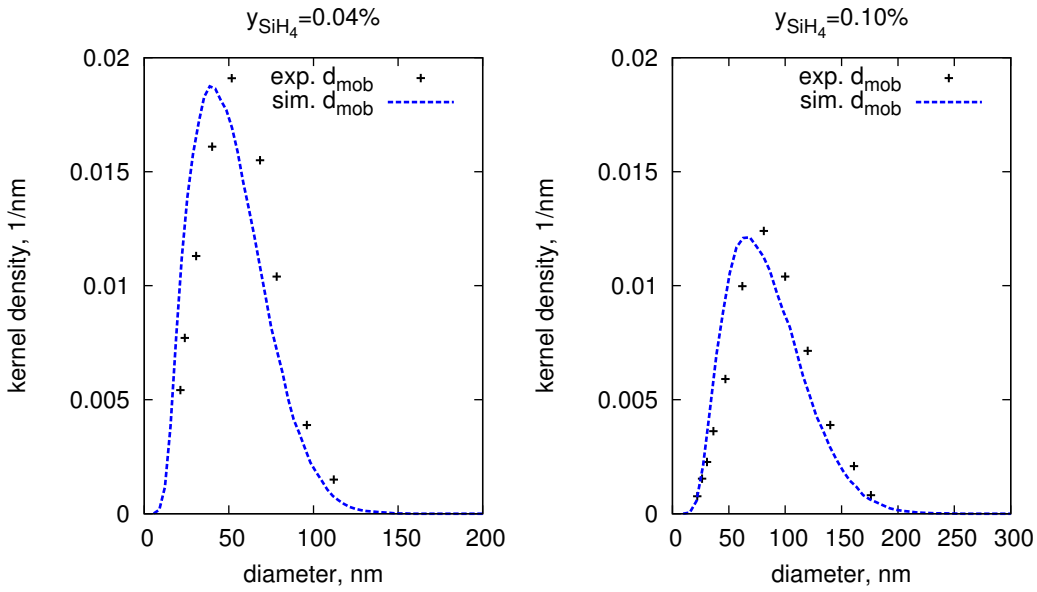

Figure 8: *Comparison of theoretical and experimental PSDs for the conditions of Nguyen and Flagan [46] with a peak reactor temperature of 800 °C.*

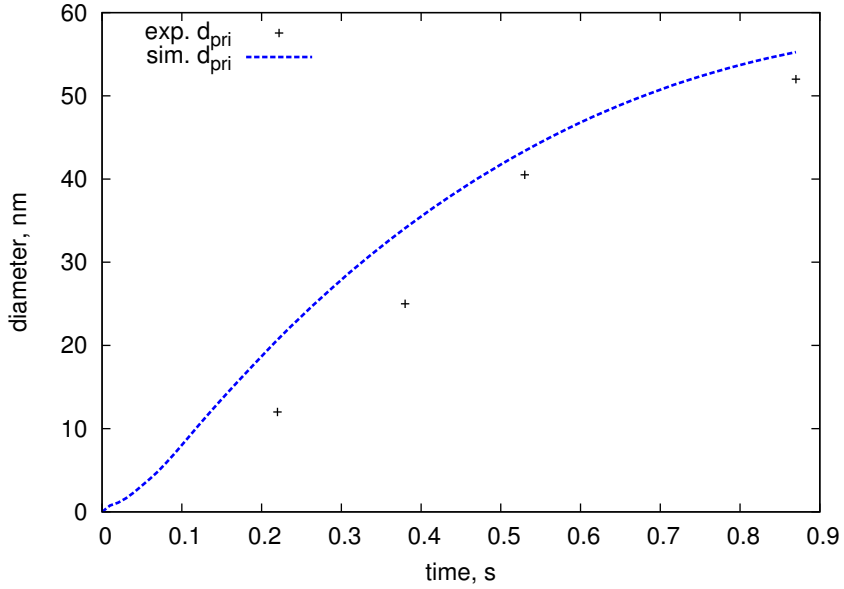

Figure 9: *Temporal evolution of the mean primary particle diameter for the conditions of Onischuk et al. [54] with initial conditions y_{SiH_4}=5% (in Ar) at 39 kPa and 580 °C.*

4.2.4 Laser synthesis of particles

Silicon particles can also be synthesised in a laser-driven flame [6, 7, 16, 17]. These studies varied process conditions such as silane fraction and cell pressure to produce highly spherical and loosely-agglomerated particles. The particle size and number density was tracked through the flame using laser-scattering measurements. To convert the temperature-length profiles given in [17], the velocity of the particles was estimated using the formula provided in [16]:

$$v = \frac{2\,Q_{\mathrm{STP}}\,T/273}{\pi\,r^2\,P_{(\mathrm{atm})}} \tag{33}$$

where Q_{STP} is the volumetric silane flow at standard temperature and pressure and r is the radius of the flame. Thus, using the velocity through the flame, the temperature-time profiles were obtained. The experimental data and model predictions for this system are supplied in Figure 11 for the 630S powder (see [17] for more information about different powder codes), assuming 109 cm^3/s of silane [17] and 400 cm^3/s of argon [6] in the inlet stream.

The present work's model gives reasonable agreement with the experimental trajectories when comparing the primary particle diameter to the experimentally observed diameter. The separation of d_{col} and d_{pri} at approximately 0.003 s represents the peak of the temperature profile, where the reaction has gone to completion and aggregates begin to form.

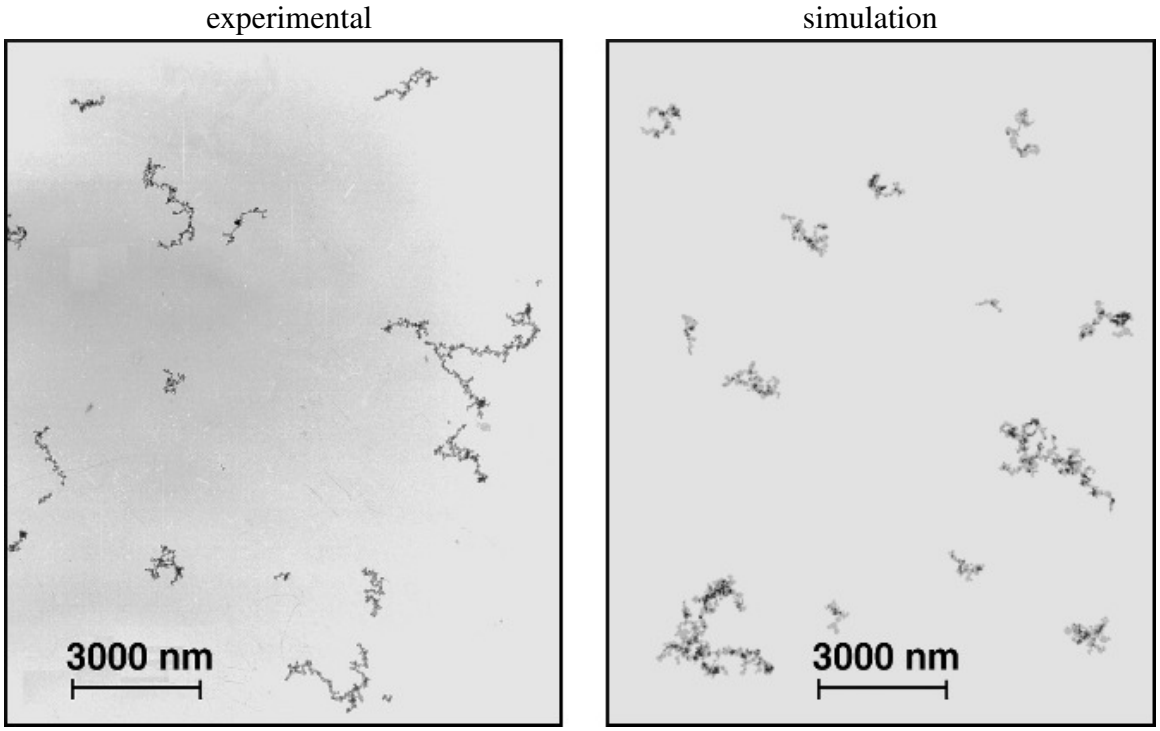

Figure 10: *An experimental TEM micrograph from the work of Onischuk et al. [54] (left panel) compared with a computer-generated TEM-style image from the present work's model (right panel) for 0.53 s reaction time followed by 17.8 s in the reactor 'cold zone'. Particle images were rendered using POV-Ray [59].*

5 Conclusions

A novel fully-coupled gas-phase and particle model for the synthesis of silicon nanoparticles was presented. The mechanism of Ho et al. [25] was used to describe the gas-phase kinetics. A multidimensional particle model tracking the number of silicon and hydrogen units of each primary particle and the connectivity of the primaries in an aggregate was used in conjunction with a stochastic population balance solver to study nanoparticle synthesis.

By adjusting the pre-exponential factors of five gas-phase and two heterogeneous reactions, good fit to a variety of experimental studies was obtained. The model was applied to different reactor configurations, process conditions and particle morphologies. Varying degrees of fit of theoretical results with experimental results were obtained, with the model generally better for atmospheric pressure cases. The robustness of this modelling methodology was demonstrated by generating a TEM-style image of silicon aggregates in qualitative agreement with experiment.

However, it was reported that in some cases where aggregate particles were produced or where large amounts of coagulation occurred, the primary diameter was larger than that observed experimentally. This was attributed to the finite-rate sintering kinetics employed. As this area is generally poorly characterised (particularly in terms of experimental work)

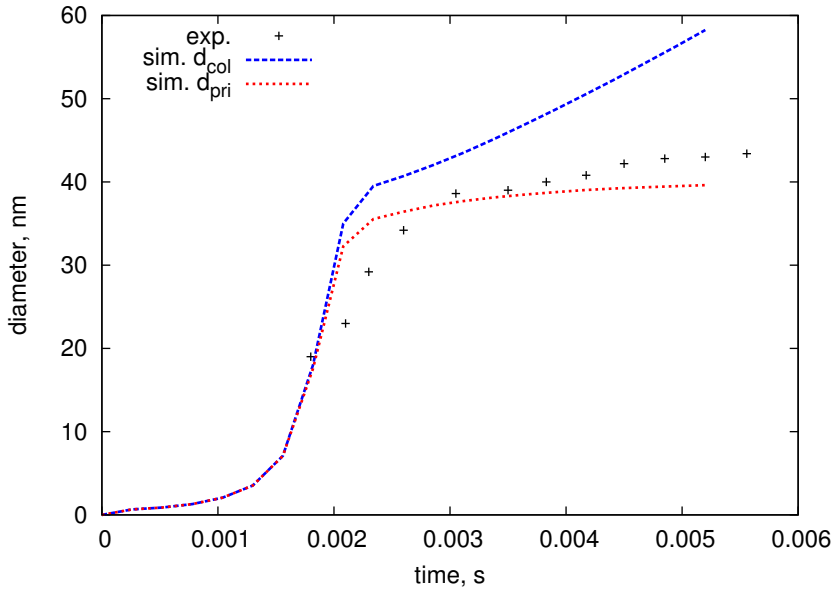

Figure 11: *Evolution of mean particle diameter for the laser-driven flame (case 630S) of Flint et al. [17] and Cannon et al. [7].*

for silicon, it is suggested that the model could be significantly improved by using an accurate sintering expression. Despite this, the model successfully knits-together many of the historical studies of silicon nanoparticle synthesis and provides a foundation on which the space of process conditions can be reliably explored.

6 Acknowledgements

W.J.M. acknowledges funding from the Cambridge Australia Trust to undertake this work. The authors additionally wish to thank the members of the Computational Modelling Group for their guidance and support. M.K. gratefully acknowledges the DFG Mercator programme and the support of CENIDE at the Unviversity of Duisburg Essen. Figure 10 (left panel) reprinted from Journal of Aerosol Science, 31, A.A. Onischuk, A.I. Levykin, V.P. Strunin, K.K. Sabelfeld, V.N. Panfilov, *Aggregate formation under homogeneous silane thermal decomposition*, 1263–1281, Copyright (2000), with permission from Elsevier.

A Conversion of *SURFACE CHEMKIN* parameters

SURFACE CHEMKIN was developed by Coltrin et al. [11] to model the complex surface chemistry in chemical vapour deposition processes. It consists of a set of packages to interpret general heterogeneous chemical mechanisms in a standardised manner. As the gas-surface mechanism proposed by Houf et al. [26] and Ho et al. [25] was formulated in terms of a *SURFACE CHEMKIN* mechanism, the form of the rate expression requires 'conversion' so that is compatible with the type-space of the present work's model.

An irreversible heterogeneous reaction may be represented in the general form [11]

$$\sum_{k=1}^{K} \nu'_k \chi_k \rightarrow \sum_{k=1}^{K} \nu''_k \chi_k \tag{A.1}$$

where ν'_k and ν''_k are the forward and reverse stoichiometric coefficients of species with chemical symbol χ_k for K chemical species. Assuming only a single irreversible heterogeneous reaction is present, the rate of progress variable q (in mol/cm^{2}s) is given by:

$$q = k_f \prod_{k=1}^{K} C_{\chi_k}^{\nu'_k} \tag{A.2}$$

where C_{χ_k} is the gas-phase (mol/cm^3) or surface (mol/cm^2) concentration of species k. The forward rate constant k_f adopts a modified-Arrhenius form

$$k_f = A^* T^{\beta} \exp\left(-\frac{E_A}{RT}\right). \tag{A.3}$$

To adapt the mechanisms for silane surface reactions [25, 26] to the present work, Equations A.1–A.3 must be applied to the chemical reactions given in Table 8.

Table 8: *Surface reaction mechanism for silanes proposed by Ho et al. [25]. The (S) and (B) subscripts refer to surface and bulk species, respectively.*

Reaction	A^* (cm^5/mol^{2}s)	β (-)	E_A (kcal/mol)
$SiH_4 + 2Si_{(S)} \rightarrow 2SiH_{(S)} + Si_{(B)} + H_2$	8.39×10^{26}	0.0	37.45
$Si_2H_6 + 2Si_{(S)} \rightarrow 2SiH_{(S)} + 2Si_{(B)} + 2H_2$	8.39×10^{27}	0.0	37.45
$Si_3H_8 + 2Si_{(S)} \rightarrow 2SiH_{(S)} + 3Si_{(B)} + 3H_2$	8.39×10^{27}	0.0	37.45

As an example, this will be done for SiH_4. Using Equation A.1, we observe that the forward rate coefficients are $\nu'_{SiH_4} = 1$ and $\nu'_{Si_{(S)}} = 2$. Thus, the rate of progress q for this reaction is given by:

$$q = A^* C_{SiH_4}^1 C_{Si_{(S)}}^2 \exp\left(-\frac{E_A}{RT}\right) \tag{A.4}$$

Writing Equation A.4 in this form enables deduction of the units of A^*. Here, they must be cm^5/mol^{2}s in order to ensure dimensional consistency. Assuming that the concentration of surface $Si_{(S)}$ sites–given by λ_{Si} (#/cm^2)–is constant, we write

$$\lambda_{Si} = N_A C_{Si_{(S)}}. \tag{A.5}$$

Table 9: *Estimation of A_{SR,SiH_4} based on different site densities.*

parameter	lower bound	this work	upper bound
λ_{Si} (#/cm^2)	8.0×10^{14} [65]	-	1.7×10^{15}
$A_{\mathrm{SR,SiH_4}}$ (cm/mol.s)	8.9×10^{32}	3.0×10^{33}	4.0×10^{33}

To 'translate' Equation A.4 to the type-space of the present work, we must ensure that the surface reaction rate R_{SR} is dimensionally consistent with the other rates:

$$R_{\mathrm{SR}} = S N_{\mathrm{A}}\, q. \tag{A.6}$$

Substituting in for λ_{Si} and rearranging yields:

$$R_{\mathrm{SR}} = A\, C_{\mathrm{SiH_4}}\, S \left(-\frac{E_{\mathrm{A}}}{RT} \right). \tag{A.7}$$

where A is the alternative pre-exponential factor used in the present work, given by:

$$A = \frac{A^* \lambda_{\mathrm{Si}}^2}{N_{\mathrm{A}}} \tag{A.8}$$

By estimating the site density λ_{Si}, it is possible to convert the value of the pre-exponential factor A^* into the A used in present work. An upper-bound on λ_{Si} can be estimated by using the bulk density of silicon. A lower bound on λ_{Si} is taken for the $\{111\}$ surface of silicon at full saturation [65].

We observe that Equation A.7 is the same as that used by Menz et al. [37]; and that the parameters for silane in Table 9 shows good agreement with their pre-exponential factors calculated via optimisation ($A_{\mathrm{SR,SiH_4}} = 3.0 \times 10^{33}$) in the present work.

References

[1] A. Adamczyk, M. Reyniers, G. Marin, and L. Broadbelt. Exploring 1, 2-hydrogen shift in silicon nanoparticles: Reaction kinetics from quantum chemical calculations and derivation of transition state group additivity database. *The Journal of Physical Chemistry A*, 113(41):10933–10946, 2009.

[2] H. Antoniadis. Silicon ink high efficiency solar cells. In *Photovoltaic Specialists Conference (PVSC), 2009 34th IEEE*, pages 650 –654, 2009.

[3] M. Bowrey and J. Purnell. The pyrolysis of disilane and rate constants of silene insertion reactions. *Proceedings of the Royal Society of London A*, 321(1546):341–359, 1971.

[4] A. Braumann, P. Man, and M. Kraft. The inverse problem in granulation modeling–Two different statistical approaches. *AIChE Journal*, 57(11):3105–3121, 2011.

[5] R. Buss, P. Ho, W. Breiland, and M. Coltrin. Reactive sticking coefficients for silane and disilane on polycrystalline silicon. *Journal of Applied Physics*, 63(8):2808–2819, 1988.

[6] W. Cannon, S. Danforth, J. Flint, J. Haggerty, and R. Marra. Sinterable ceramic powders from laser-driven reactions: I, Process description and modeling. *Journal of the American Ceramic Society*, 65(7):324–330, 1982.

[7] W. Cannon, S. Danforth, J. Haggerty, and R. Marra. Sinterable ceramic powders from laser-driven reactions: II, Powder characteristics and process variables. *Journal of the American Ceramic Society*, 65(7):330–335, 1982.

[8] M. Celnik, R. Patterson, M. Kraft, and W. Wagner. Coupling a stochastic soot population balance to gas-phase chemistry using operator splitting. *Combustion and Flame*, 148(3):158–176, 2007.

[9] M. Celnik, R. Patterson, M. Kraft, and W. Wagner. A predictor-corrector algorithm for the coupling of stiff ODEs to a particle population balance. *Journal of Computational Physics*, 228(8):2758–2769, 2009.

[10] D. Chen, Z. Zainuddin, E. Yapp, J. Akroyd, S. Mosbach, and M. Kraft. A fully coupled simulation of PAH and soot growth with a population balance model. *Proceedings of the Combustion Institute*, In press.

[11] M. Coltrin, R. Kee, F. Rupley, and E. Meeks. SURFACE CHEMKIN III: A Fortran Package for Analyzing Heterogeneous Chemical Kinetics at a Solid-Surface-Gas-Phase Interface. *Sandia National Laboratories Report SAND96-8217*, 1996.

[12] H. Dang and M. Swihart. Computational modeling of silicon nanoparticle synthesis: I. A general two-dimensional model. *Aerosol Science and Technology*, 43(3):250–263, 2009.

[13] H. Dang and M. Swihart. Computational modeling of silicon nanoparticle synthesis: II. A two-dimensional bivariate model for silicon nanoparticle synthesis in a laser-driven reactor including finite-rate coalescence. *Aerosol Science and Technology*, 43 (6):554–569, 2009.

[14] M. Eggersdorfer, D. Kadau, H. Herrmann, and S. Pratsinis. Aggregate morphology evolution by sintering: Number & diameter of primary particles. *Journal of Aerosol Science*, 46:7–19, 2012.

[15] F. Eversteijn. Gas-phase decomposition of silane in a horizontal epitaxial reactor. *Philips Res. Repts*, 26(2):134–144, 1971.

[16] J. Flint and J. Haggerty. A model for the growth of silicon particles from laser-heated gases. *Aerosol Science and Technology*, 13(1):72–84, 1990.

[17] J. Flint, R. Marra, and J. Haggerty. Powder temperature, size, and number density in laser-driven reactions. *Aerosol Science and Technology*, 5(2):249–260, 1986.

[18] M. Frenklach, L. Ting, H. Wang, and M. Rabinowitz. Silicon particle formation in pyrolysis of silane and disilane. *Israel Journal of Chemistry*, 36(3):293–303, 1996.

[19] B. Giesen, H. Wiggers, A. Kowalik, and P. Roth. Formation of Si-nanoparticles in a microwave reactor: Comparison between experiments and modelling. *Journal of Nanoparticle Research*, 7(1):29–41, 2005.

[20] C. Giunta, R. McCurdy, J. Chapple-Sokol, and R. Gordon. Gas-phase kinetics in the atmospheric pressure chemical vapor deposition of silicon from silane and disilane. *Journal of Applied Physics*, 67(2):1062–1075, 1990.

[21] D. Gray, editor. *American Institute of Physics Handbook*. McGraw-Hill, New York, 1972.

[22] M. Gröschel, R. Körmer, M. Walther, G. Leugering, and W. Peukert. Process control strategies for the gas phase synthesis of silicon nanoparticles. *Chemical Engineering Science*, 73:181–194, 2012.

[23] A. Gupta and H. Wiggers. Surface chemistry and photoluminescence property of functionalized silicon nanoparticles. *Physica E*, 41(6):1010–1014, 2009.

[24] T. Hirokami, Y. Maeda, and H. Tsukada. Parameter estimation using simultaneous perturbation stochastic approximation. *Electrical Engineering in Japan*, 154:30–39, 2006.

[25] P. Ho, M. Coltrin, and W. Breiland. Laser-induced fluorescence measurements and kinetic analysis of Si atom formation in a rotating disk chemical vapor deposition reactor. *The Journal of Physical Chemistry*, 98(40):10138–10147, 1994.

[26] W. Houf, J. Grcar, and W. Breiland. A model for low pressure chemical vapor deposition in a hot-wall tubular reactor. *Materials Science and Engineering: B*, 17 (1-3):163–171, 1993.

[27] J. Knipping, H. Wiggers, B. Rellinghaus, P. Roth, D. Konjhodzic, and C. Meier. Synthesis of high purity silicon nanoparticles in a low pressure microwave reactor. *Journal of Nanoscience and Nanotechnology*, 4(8):1039–1044, 2004.

[28] A. Kobata, K. Kusakabe, and S. Morooka. Growth and transformation of TiO_2 crystallites in aerosol reactor. *AIChE journal*, 37(3):347–359, 1991.

[29] W. Koch and S. Friedlander. The effect of particle coalescence on the surface area of a coagulating aerosol. *Journal of Colloid and Interface Science*, 140(2):419–427, 1990.

[30] R. Körmer, M. Jank, H. Ryssel, H. Schmid, and W. Peukert. Aerosol synthesis of silicon nanoparticles with narrow size distribution–Part 1: Experimental investigations. *Journal of Aerosol Science*, 41(11):998–1007, 2010.

[31] R. Körmer, H. Schmid, and W. Peukert. Aerosol synthesis of silicon nanoparticles with narrow size distribution–Part 2: Theoretical analysis of the formation mechanism. *Journal of Aerosol Science*, 41(11):1008–1019, 2010.

[32] M. Koshi, S. Kato, and H. Matsui. Unimolecular decomposition of silane, fluorosilane, and difluorosilane at high temperatures. *The Journal of Physical Chemistry*, 95 (3):1223–1227, 1991.

[33] F. Kruis, K. Kusters, S. Pratsinis, and B. Scarlett. A simple model for the evolution of the characteristics of aggregate particles undergoing coagulation and sintering. *Aerosol Science and Technology*, 19:514–526, 1993.

[34] F. Kruis, J. Schoonman, and B. Scarlett. Homogeneous nucleation of silicon. *Journal of Aerosol Science*, 25(7):1291–1304, 1994.

[35] Z. Li and E. Ruckenstein. Water-soluble poly (acrylic acid) grafted luminescent silicon nanoparticles and their use as fluorescent biological staining labels. *Nano Letters*, 4(8):1463–1467, 2004.

[36] W. Menz, R. Patterson, W. Wagner, and M. Kraft. Application of stochastic weighted algorithms to a multidimensional silica particle model. *Journal of Computational Physics*, (submitted for review).

[37] W. Menz, S. Shekar, G. Brownbridge, S. Mosbach, R. Körmer, W. Peukert, and M. Kraft. Synthesis of silicon nanoparticles with a narrow size distribution: a theoretical study. *Journal of Aerosol Science*, 44:46–61, 2012.

[38] M. Meunier, J. Flint, J. Haggerty, and D. Adler. Laser-induced chemical vapor deposition of hydrogenated amorphous silicon. I. Gas-phase process model. *Journal of Applied Physics*, 62(7):2812–2821, 1987.

[39] M. Meunier, J. Flint, J. Haggerty, and D. Adler. Laser-induced chemical vapor deposition of hydrogenated amorphous silicon. II. Film properties. *Journal of Applied Physics*, 62(7):2821–2829, 1987.

[40] N. Morgan, C. Wells, M. Kraft, and W. Wagner. Modelling nanoparticle dynamics: coagulation, sintering, particle inception and surface growth. *Combustion Theory and Modelling*, 9(3):449–461, 2005.

[41] N. Morgan, C. Wells, M. Goodson, M. Kraft, and W. Wagner. A new numerical approach for the simulation of the growth of inorganic nanoparticles. *Journal of Computational Physics*, 211(2):638–658, 2006.

[42] N. Morgan, M. Kraft, M. Balthasar, D. Wong, M. Frenklach, and P. Mitchell. Numerical simulations of soot aggregation in premixed laminar flames. *Proceedings of the Combustion Institute*, 31(1):693–700, 2007.

[43] S. Mosbach, A. Braumann, P. Man, C. Kastner, G. Brownbridge, and M. Kraft. Iterative improvement of bayesian parameter estimates for an engine model by means of experimental design. *Combustion and Flame*, pages 1303–1313, 2012.

[44] T. Murthy, N. Miyamoto, M. Shimbo, and J. Nishizawa. Gas-phase nucleation during the thermal decomposition of silane in hydrogen. *Journal of Crystal Growth*, 33 (1):1–7, 1976.

[45] O. Nayfeh, D. Antoniadis, K. Mantey, and M. Nayfeh. Memory effects in metal-oxide-semiconductor capacitors incorporating dispensed highly monodisperse 1 nm silicon nanoparticles. *Applied Physics Letters*, 90(15):153105–153105, 2007.

[46] H. Nguyen and R. Flagan. Particle formation and growth in single-stage aerosol reactors. *Langmuir*, 7(8):1807–1814, 1991.

[47] S. Nijhawan, P. McMurry, M. Swihart, S. Suh, S. Girshick, S. Campbell, and J. Brockmann. An experimental and numerical study of particle nucleation and growth during low-pressure thermal decomposition of silane. *Journal of Aerosol Science*, 34(6):691–711, 2003.

[48] J. Odden, P. Egeberg, and A. Kjekshus. From monosilane to crystalline silicon, Part I: Decomposition of monosilane at 690–830 K and initial pressures 0.1–6.6 MPa in a free-space reactor. *Solar Energy Materials and Solar Cells*, 86(2):165–176, 2005.

[49] J. Odden, P. Egeberg, and A. Kjekshus. From monosilane to crystalline silicon, Part III. Characterization of amorphous, hydrogen-containing silicon products. *Journal of Non-Crystalline Solids*, 351(14):1317–1327, 2005.

[50] J. Odden, P. Egeberg, and A. Kjekshus. From monosilane to crystalline silicon, Part II: Kinetic considerations on thermal decomposition of pressurized monosilane. *International Journal of Chemical Kinetics*, 38(5):309–321, 2006.

[51] A. Onischuk, V. Strunin, R. Samoilova, A. Nosov, M. Ushakova, and V. Panfilov. Chemical composition and bond structure of aerosol particles of amorphous hydrogenated silicon forming from thermal decomposition of silane. *Journal of Aerosol Science*, 28(8):1425–1441, 1997.

[52] A. Onischuk, V. Strunin, M. Ushakova, and V. Panfilov. On the pathways of aerosol formation by thermal decomposition of silane. *Journal of Aerosol Science*, 28(2): 207–222, 1997.

[53] A. Onischuk, V. Strunin, M. Ushakova, and V. Panfilov. Studying of silane thermal decomposition mechanism. *International Journal of Chemical Kinetics*, 30(2):99–110, 1998.

[54] A. Onischuk, A. Levykin, V. Strunin, K. Sabelfeld, and V. Panfilov. Aggregate formation under homogeneous silane thermal decomposition. *Journal of Aerosol Science*, 31(11):1263–1281, 2000.

[55] A. Onischuk, A. Levykin, V. Strunin, M. Ushakova, R. Samoilova, K. Sabelfeld, and V. Panfilov. Aerosol formation under heterogeneous/homogeneous thermal decomposition of silane: experiment and numerical modeling. *Journal of Aerosol Science*, 31(8):879–906, 2000.

[56] R. Patterson and M. Kraft. Models for the aggregate structure of soot particles. *Combustion and Flame*, 151(1-2):160–172, 2007.

[57] R. Patterson, J. Singh, M. Balthasar, M. Kraft, and J. Norris. The linear process deferment algorithm: A new technique for solving population balance equations. *SIAM Journal on Scientific Computing*, 28(1):303, 2006.

[58] H. Paur, W. Baumann, H. Mätzing, and H. Seifert. Formation of nanoparticles in flames; measurement by particle mass spectrometry and numerical simulation. *Nanotechnology*, 16:S354, 2005.

[59] Persistence of Vision Pty. Ltd. Persistence of Vision Raytracer (Version 3.6), 2004. URL http://www.povray.org/.

[60] E. Petersen and M. Crofton. Measurements of high-temperature silane pyrolysis using SiH_4 IR emission and SiH_2 laser absorption. *The Journal of Physical Chemistry A*, 107(50):10988–10995, 2003.

[61] J. Purnell and R. Walsh. The pyrolysis of monosilane. *Proceedings of the Royal Society of London A*, 293(1435):543–561, 1966.

[62] S. Rogak, R. Flagan, and H. Nguyen. The mobility and structure of aerosol agglomerates. *Aerosol Science and Technology*, 18(1):25–47, 1993.

[63] M. Sander, R. West, M. Celnik, and M. Kraft. A detailed model for the sintering of polydispersed nanoparticle agglomerates. *Aerosol Science and Technology*, 43(10): 978–989, 2009.

[64] M. Sander, R. Patterson, A. Braumann, A. Raj, and M. Kraft. Developing the PAH-PP soot particle model using process informatics and uncertainty propagation. *Proceedings of the Combustion Institute*, 33(1):675–683, 2011.

[65] G. Schulze and M. Henzler. Adsorption of atomic hydrogen on clean cleaved silicon (111). *Surface Science*, 124(2):336–350, 1983.

[66] S. Shekar, M. Sander, R. Riehl, A. Smith, A. Braumann, and M. Kraft. Modelling the flame synthesis of silica nanoparticles from tetraethoxysilane. *Chemical Engineering Science*, 70:54–66, 2011.

[67] S. Shekar, W. Menz, A. Smith, M. Kraft, and W. Wagner. On a multivariate population balance model to describe the structure and composition of silica nanoparticles. *Computers & Chemical Engineering*, 43:130–147, 2012.

[68] S. Shekar, A. Smith, W. Menz, M. Sander, and M. Kraft. A multidimensional population balance model to describe the aerosol synthesis of silica nanoparticles. *Journal of Aerosol Science*, 44:83–98, 2012.

[69] B. Silverman. *Density estimation for statistics and data analysis*. Chapman & Hall/CRC, 1986.

[70] K. Sinniah, M. Sherman, L. Lewis, W. Weinberg, J. Yates Jr, and K. Janda. Hydrogen desorption from the monohydride phase on Si (100). *The Journal of Chemical Physics*, 92:5700, 1990.

[71] M. Swihart and S. Girshick. Thermochemistry and kinetics of silicon hydride cluster formation during thermal decomposition of silane. *The Journal of Physical Chemistry B*, 103(1):64–76, 1999.

[72] S. Vepřek, K. Schopper, O. Ambacher, W. Rieger, and M. Vepřek-Heijman. Mechanism of cluster formation in a clean silane discharge. *Journal of The Electrochemical Society*, 140:1935, 1993.

[73] R. West, R. Shirley, M. Kraft, C. Goldsmith, and W. Green. A detailed kinetic model for combustion synthesis of titania from $TiCl_4$. *Combustion and Flame*, 156: 1764–1770, 2009.

[74] D. Woiki, L. Catoire, and P. Roth. High-temperature kinetics of Si-containing precursors for ceramic processing. *AIChE Journal*, 43(S11):2670–2678, 1997.

[75] H. Wong, X. Li, M. Swihart, and L. Broadbelt. Detailed kinetic modeling of silicon nanoparticle formation chemistry via automated mechanism generation. *The Journal of Physical Chemistry A*, 108(46):10122–10132, 2004.

[76] J. Wu and R. Flagan. Onset of runaway nucleation in aerosol reactors. *Journal of Applied Physics*, 61(4):1365–1371, 1987.

[77] J. Wu, R. Flagan, and O. Gregory. Submicron silicon powder production in an aerosol reactor. *Applied Physics Letters*, 49(2):82–84, 1986.

[78] J. Wu, H. Nguyen, and R. Flagan. A method for the synthesis of submicron particles. *Langmuir*, 3(2):266–271, 1987.

[79] M. Zachariah and M. Carrier. Molecular dynamics computation of gas-phase nanoparticle sintering: a comparison with phenomenological models. *Journal of Aerosol Science*, 30:1139–1152, 1999.